International Journal of Engineering Science 224 (2026) 104531

Contents lists available at ScienceDirect

International Journal of Engineering Science

journal homepage: www.elsevier.com/locate/ijengsci

Full Length Article

Type-II hyperbolic lattices for elastic wave manipulations

Kailun Wang [a,1], Jingming Chen [b,1], Yue Shen [a], Xiang Li [c,**], Zhen Gao [b,**], Ying Wu [a,*]

[a] School of Physics, Nanjing University of Science and Technology, Nanjing 210094, China
[b] State Key Laboratory of Optical Fiber and Cable Manufacturing Technology, Department of Electronic and Electrical Engineering, Guangdong Key Laboratory of Integrated Optoelectronics Intellisense, Southern University of Science and Technology, Shenzhen 518055, China
[c] School of Physics and Mechanics, Wuhan University of Science and Technology, Wuhan 430065, China

ARTICLE INFO

Keywords:
Type II Hyperbolic Lattices
Elastic Metamaterials
Wave Manipulation
Edge States

ABSTRACT

Hyperbolic lattices, as representative non-Euclidean structures, offer unique opportunities for controlling elastic wave propagation. In this paper, we theoretically, numerically, and experimentally investigate boundary-localized wave behavior in type-II hyperbolic lattices. Derived from a low-dimensional mapping of hyperbolic space, these lattices naturally feature distinct inner and outer boundaries. The spatial modulation of the hyperbolic metric induces boundary localization through geometric regulation. Eigenfrequency analysis reveals that elastic wave energy concentrates along either the inner or outer boundaries within specific frequency ranges. Combined steady-state and transient experiments confirm these localized edge phenomena, quantified using boundary polarization indices. These results elucidate the mechanism of boundary-dominated wave manipulation in type-II hyperbolic lattices, offering new insights for the design of non-Euclidean metamaterials with potential applications in impact protection, energy absorption, and harvesting.

1. Introduction

Lattice metamaterials have long been a research focus in the field of mechanics (Ren et al., 2018, Li et al., 2024, Ma et al., 2025). Through the elaborate design of unit cells and strategic integration, researchers aim to endow lattice materials with multi-dimensional mechanical properties (Wang et al., 2020, Song et al., 2024, Fang et al., 2025) for diverse structural and energy-absorbing applications, and topological properties (Yang et al., 2022, Wu et al., 2023, Cui et al., 2024) for robust wave manipulations. Nevertheless, most of these structures are developed within the Euclidean space, focusing on flat and curved geometric structures (Waitukaitis et al., 2020, Dang et al., 2022, Hong et al., 2022). Essentially, they are different embeddings of two-dimensional (2D) manifolds in Euclidean space. The Gaussian curvatures of these structures can be classified as zero, positive, and negative, respectively. However, the negative curvature is only locally rather than globally defined geometric configurations (Chen et al., 2022, Zheng & Chen, 2023), with such structures exhibiting local negative curvature in Euclidean space. This geometric constraint not only limits the exploration of new non-Euclidean structures but also hinders the widespread applications of curved regulations.

In the past decade, attention has been toward non-Euclidean geometric structures with constant negative curvature (Tung, 2018,

* Corresponding author.
** Co-corresponding authors.
E-mail addresses: xli@wust.edu.cn (X. Li), gaoz@sustech.edu.cn (Z. Gao), yingwu@njust.edu.cn (Y. Wu).
[1] These authors contributed equally to this work.

https://doi.org/10.1016/j.ijengsci.2026.104531
Received 8 February 2026; Received in revised form 4 March 2026; Accepted 12 March 2026

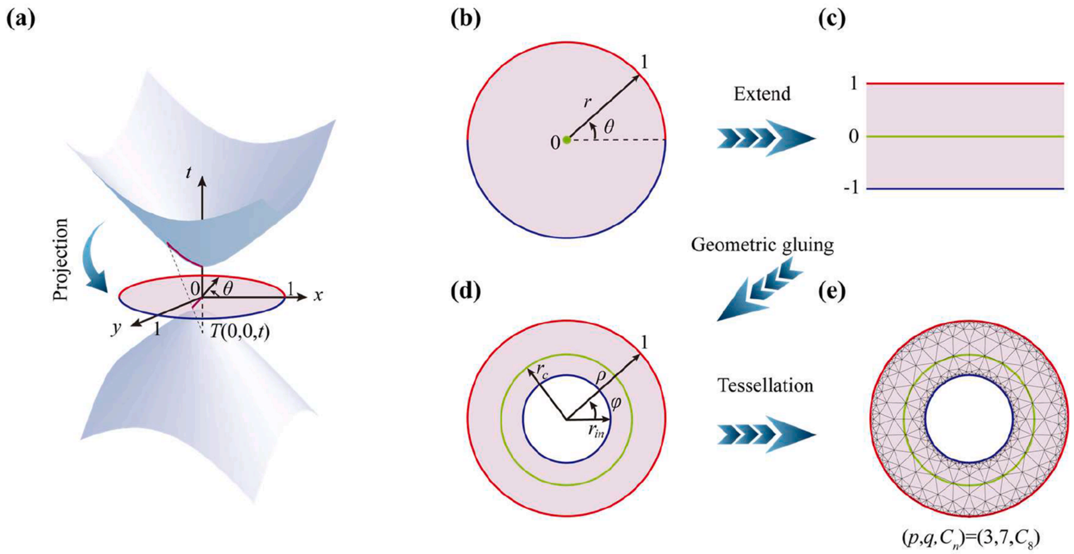

Fig. 1. Generation of type-II hyperbolic lattices. (a) The projection of the one-sheeted hyperboloid in (2+1) -dimensional Minkowski space onto the Poincaré disk. (b) The Poincaré disk with $r = 1$. The red line represents the upper boundary of the disk, the blue line represents the lower boundary of the disk, and the green dot represents the origin. (c) The Poincaré disk extends into hyperbolic band. (d) Hyperbolic ring, where $r_c = e^{-\pi/(2r_h)}$, $r_{in} = e^{-\pi/r_h}$, $r_h = 3.69$. (e) $\{3, 7, C_8\}$ type-II hyperbolic lattice.

Tung & Weinmüller, 2019, Lei et al., 2025). In particular, hyperbolic space, in contrast to the flat nature of Euclidean space, exhibits a constant negative spatial curvature, within which the parallel axiom of Euclidean geometry ceases to hold (Harvey, 2016). Endowed with infinite divergent properties, it has emerged as a pivotal tool for elucidating general relativity and black hole theory (Bañados et al., 1992, Wang & Ren, 2023). However, according to Hilbert's theorem (Hilbert, 1890), a complete, smooth surface with constant negative Gaussian curvature cannot be isometrically embedded in 3D Euclidean space. It is difficult to directly introduce hyperbolic space into reality to construct wave models. Consequently, researchers have resorted to embedding the hyperbolic sheet into a 2D Euclidean disk via projection mapping, which is the Poincaré disk (Anderson, 2005). When utilizing regular polygons for tessellation discretization of the disk, type-I hyperbolic lattices can be formulated (Kollár et al., 2019). By virtue of the negative-curvature properties, type-I hyperbolic lattices have exhibited novel physical characteristics in various fields such as crystal band theory (Maciejko & Rayan, 2021, Boettcher et al., 2022, Cheng et al., 2022), quantum electrodynamics (Kollár et al., 2020, Boettcher et al., 2020, Bienias et al., 2022), topological circuits (Zhang et al., 2022, Chen et al., 2023, Zhang et al., 2023, Chen et al., 2024, Yuan et al., 2024), and topological optical insulators (Huang et al., 2024, Qin et al., 2024, Huang et al., 2025). In the field of elastic waves, type-I lattices can regulate wave propagation through the geometric metric, enabling the structures to exhibit high-density boundary states in the vibration spectra, which open new avenues for energy absorption and vibration isolation in engineering (Ruzzene et al., 2021, Patino et al., 2024, Patino et al., 2025).

Recently, type-II hyperbolic lattices have been proposed (Chen et al., 2023, Dey et al., 2024), which generate topologically consistent inner and outer boundaries by conformal transformations, providing a new ideal platform for investigations of hyperbolic systems. For example, Chen et al (Chen et al., 2025) have designed type-II hyperbolic circuit Chern insulators that support counter-propagating chiral edge states at both inner and outer edges, offering new possibilities for constructing robust and miniaturized quantum devices. However, type-II lattices for elastic wave manipulations remain unreported. Such a unique geometry dominated by dual boundaries tends to induce localized vibration modes, diverse edge states, thereby further advancing non-Euclidean geometric theory in the field of elastic metamaterials.

Here, we investigate the characteristics of elastic waves in type-II hyperbolic lattices, including aggregation of boundary states in the eigenspectra and transient responses of structure vibration marginalization. We first conduct a conformal transformation on type-I lattices and convert them into type-II hyperbolic lattices with inner and outer boundaries. Next, we calculate the out-of-plane mode eigenspectra and analyze the transient responses by using pulse excitation. The results show that elastic waves in type-II hyperbolic lattices can be regulated at the boundaries due to the geometric metric modulation of hyperbolic space. More importantly, these boundary waves gradually dissipate the excitation energy along the edges, which implies that the structure is expected to provide new design ideas for engineering materials in the fields of impact resistance and protection.

2. Hyperbolic geometry in type-II hyperbolic lattices

We start by focusing on the one-sheeted hyperboloid in $(2+1)$-dimensional Minkowski space ($t^2 - x^2 - y^2 = 1$). By passing through the point $(0,\ 0,\ t)$, where $t = -1$, we can project hyperbolic space onto the Poincaré disk ($\mathscr{D} = \{z = re^{I\theta},\ r < 1\},\ \ I = \sqrt{-1}$)

in the plane (at $t = 0$), as shown in Fig. 1(a). The geometric metric on the Poincaré disk satisfies (Poincaré, 1882):

$$\mathrm{d}s^2 = -\frac{4\left(\mathrm{d}r^2 + r^2\mathrm{d}\theta^2\right)}{\kappa(1-r^2)^2} \tag{1}$$

where ds denotes the line element on the Poincaré disk with Gaussian curvature κ ($\kappa = -1$ for hyperbolic space with constant negative curvature (Berger, 2003)). Compared to the Euclidean metric $\mathrm{d}s^2 = \mathrm{d}r^2 + r^2\mathrm{d}\theta^2$, geometric lines are distorted under the hyperbolic metric. In the Poincaré disk, hyperbolic distance grows exponentially as one approaches the boundary. While the disk's central region ($r\rightarrow0$) approximates Euclidean geometry, infinitesimal Euclidean distances near its boundary ($r\rightarrow1$) exhibit a mapping to unbounded hyperbolic distances. This enables such a bounded disk to simulate the infinite hyperbolic space.

Applying conformal transformations (see Appendix A), we can map the Poincaré disk (Fig. 1(b)) to hyperbolic band (Fig. 1(c)) and hyperbolic ring (Fig. 1(d)). The geometric metric of the hyperbolic ring as Eq. (2):

$$\mathrm{d}s^2 = -\frac{r_h^2(\mathrm{d}\rho^2 + \rho^2\mathrm{d}\varphi^2)}{\kappa\rho^2\sin^2(r_h\ln\rho)}, r_{in} = e^{-\frac{\pi}{r_h}} < \rho < 1 \tag{2}$$

where $w = \rho e^{I\varphi}$ is the point on the ring, $\kappa = -1$, $r_h = nP/4$ ($P = 1.845$) is used to adjust the rotational symmetry of the ring by modifying different P and n-fold rotational symmetry. Eq. (2) shows that when $\rho\rightarrow1$ or $\rho\rightarrow r_{in}$, the hyperbolic ring metric diverges, generating two infinitely distant boundaries. This creates one more boundary than the Poincaré disk, endowing the structure with the possibility of multiple vibration modes. Further, we use regular polygons for tiling to form type-II hyperbolic lattices (Fig. 1 (e)).

In addition, to facilitate the classification of discretized hyperbolic lattices, we use the Schläfli symbol (Coxeter, 1988) $\{p, q\}$ to represent different types of lattices, which means q regular-p-polygons meeting at a vertex. In hyperbolic space, due to the constant negative curvature, p and q satisfy $(p-2)(q-2) > 4$, which has infinitely many solutions theoretically. Thus, for the hyperbolic plane, an infinite number of types of tilings are allowed. For type-II hyperbolic lattices, we additionally introduce C_n to represent the n-fold rotational symmetry of the lattice. Then, the symbol is denoted as $\{3, 7, C_8\}$ in our structure.

3. Analysis of wave modes in hyperbolic ring

Consider the wave equation of a 2D plane in Euclidean space:

$$\frac{1}{c_0^2}\frac{\partial^2 u(r,\theta)}{\partial t^2} - \Delta_E u(r,\theta) = 0 \tag{3}$$

where $\Delta_E = \partial^2/\partial r^2 + \left(\partial^2/\partial r\right)/r + \left(\partial^2/\partial\theta^2\right)/r^2$ is the Laplacian operator in Euclidean space, $u(r,\theta)$ denotes the displacement. We consider out-of-plane elastic wave modes in solid elastic media so the wave velocity $c_0 = \sqrt{E/[2\rho_0(1+\mu)]}$, where E, ρ_0 and μ correspond to the elastic modulus, mass density and Poisson's ratio of the material, respectively. To accurately describe the elastic wave behavior in hyperbolic space, we must introduce the hyperbolic metric to modify the differential operator of the wave equation. Nevertheless, this modification is only to adapt to the geometric characteristics of hyperbolic space and introduce effects at the geometric level, which does not change the essence of the equation based on the linear elastic constitutive relation. However, the Laplacian operator in hyperbolic space differs fundamentally from its Euclidean counterpart. Its expression varies with the coordinate system employed and the specific model of hyperbolic space adopted. Therefore, we consider the general form of the Laplace operator on a Riemannian manifold as

$$\Delta_g = \frac{1}{\sqrt{|g|}}\sum_{i,j}\frac{\partial}{\partial x_i}\left(\sqrt{|g|}\,g^{ij}\frac{\partial}{\partial x_j}\right) \tag{4}$$

where g denotes the metric tensor on the manifold, g^{ij} is the inverse of g_{ij}. In Euclidean space, the metric tensor $g_E = \delta_{ij}$, $\Delta_g = \Delta_E$ such is the usual Laplace operator.

Within the Poincaré disk, the solution to Eq. (3) can be derived through the substitution of the metric presented in Eq. (1) (Lenggenhager et al., 2022, Petermann & Hinrichsen, 2024):

$$u(r,\theta) = P_{l_D}^{m_D}\left(\frac{1+r^2}{1-r^2}\right)e^{Im_D\theta} \tag{5}$$

where m_D and l_D are two parameters of the associated Legendre functions. $l_D = -1/2(1+Ik)$, $k^2 + 1 = 4\omega_D^2/c_0^2$, ω_D is the angular frequency. We now examine the hyperbolic ring metric as presented in Eq. (2), from which the generalized Laplacian operator can be derived Δ_R,

$$\Delta_R = \frac{\rho^2\sin^2(r_h\ln\rho)}{r_h^2}\Delta_E \tag{6}$$

By modifying Eq. (3) with Δ_R, we obtain the wave equation in the hyperbolic ring,

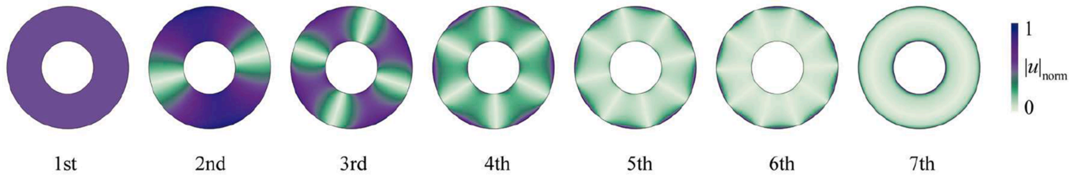

Fig. 2. Distribution of the first seven hyperbolic modes in the continuum.

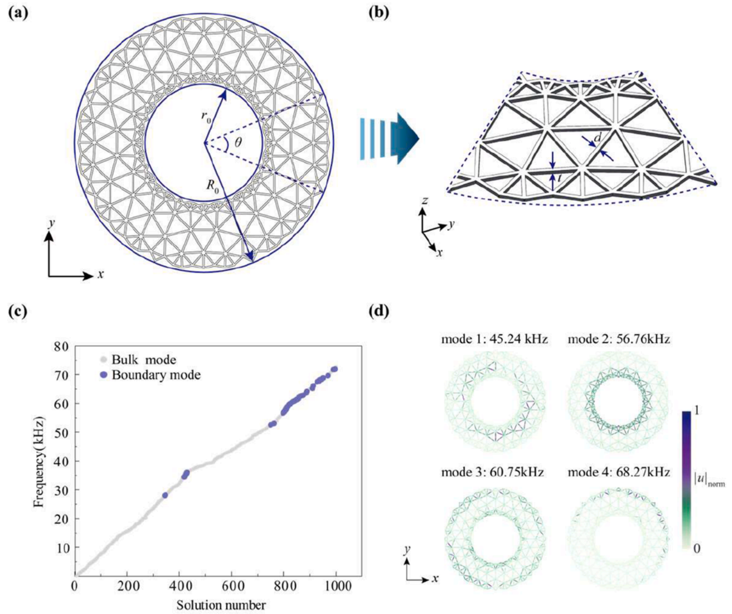

Fig. 3. Type-II hyperbolic ring out-of-plane model and eigenspectrum. (a) $\{3, 7, C_8\}$ type-II lattice model with $r_0 = 81.2$ mm, $R_0 = 174.9$ mm, $\theta = \pi/4$. (b) $1/8$ unit of the lattice with $t = 4$ mm, $d = 2$ mm. (c) The eigenspectrum of the model. (d) Normalized displacement ($|u|_{\text{norm}}$) fields of four different modes. Mode 1 is bulk mode, mode 2 is inner boundary mode, mode 3 is inner and outer mixed boundary mode, mode 4 is outer boundary mode.

$$\frac{1}{c_0^2}\frac{\partial^2 u(\rho,\varphi)}{\partial t^2} - \frac{\rho^2 \sin^2(r_h \ln\rho)}{r_h^2}\Delta_E u(\rho,\varphi) = 0 \tag{7}$$

Considering the solution $\partial^2 u(\rho,\varphi)/\partial t^2 = -\omega^2 u(\rho,\varphi)$, Eq. (7) can be written as

$$\left[\frac{\rho^2 \sin^2(r_h \ln\rho)}{r_h^2}\Delta_E + \frac{\omega^2}{c_0^2}\right]u(\rho,\varphi) = 0 \tag{8}$$

Eq. (8) is the eigenvalue equation corresponding to the wave equation in the Poincaré ring. Separating the variables $u(\rho,\varphi) = y(\varphi)g(\rho)$, Eq. (8) can be written as:

$$-\frac{y''(\varphi)}{y(\varphi)} = \frac{\rho^2 g''(\rho) + \rho g'(\rho)}{g(\rho)} + \frac{\omega^2 r_h^2}{c_0^2 \sin^2(r_h \ln\rho)} \tag{9}$$

Set $y(\varphi) = e^{Im\varphi}$, $k = \cos(r_h \ln\rho)$, and we can obtain the following equation,

$$(1-k^2)g''(k) - kg'(k) + \left[\frac{\omega^2}{c_0^2(1-k^2)} - m^2 \Big/ r_h^2\right]g(k) = 0 \tag{10}$$

Eq. (10) is the associated Legendre equation, and its standard solutions are

$$u(\rho,\varphi) = \left[\cos^2(r_h \ln\rho) - 1\right]^{1/4} P_l^{\not{\varphi}}[\cos(r_h \ln\rho)]e^{Im\varphi} \tag{11}$$

where $P_l^{\not{\varphi}}(k)$ is the Legendre function, $l = I(I + 2m/r_h)/2$, $\not{\varphi} = \left(\sqrt{1 - 4\omega^2/c_0^2}\right)/2$.

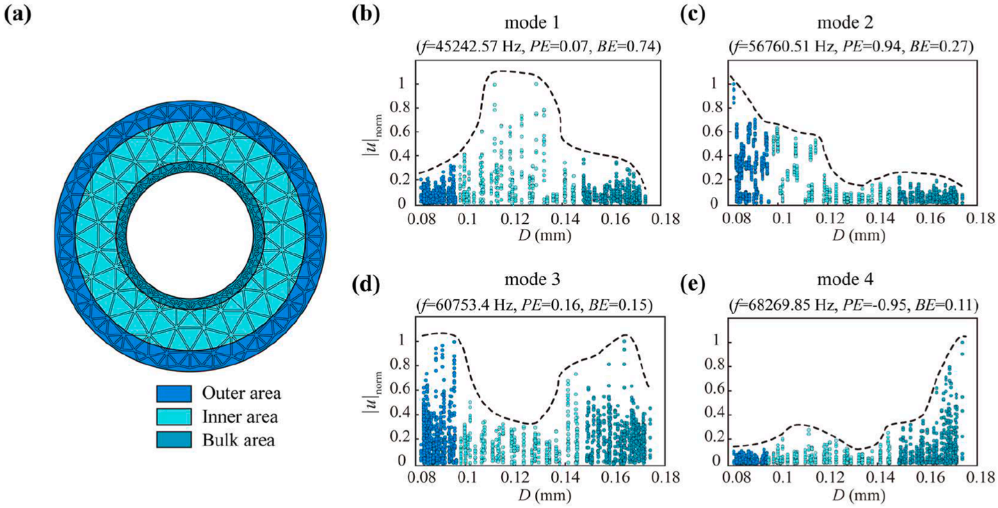

Fig. 4. The division of the structure into three regions and the boundary state indices of four modes. (a) Mode 1 is the bulk area, with $PE = 0.07$ and $BE = 0.74$. (b) Mode 2 is the inner area, with $PE = 0.94$ and $BE = 0.27$. (c) Mode 3 is the inner and outer mixed area, with $PE = 0.16$ and $BE = 0.15$. (d) Mode 4 is the outer area, with $PE = -0.95$ and $BE = 0.11$.

Given that $P_l^{\gamma}(k)$ is the associated Legendre function with complex parameters, it is reminiscent of eigenmodes with radial oscillation patterns. The first seven eigenmodes of the continuum (Fig. 2) are computed using the PDE module in COMSOL Multiphysics without additional boundary conditions. In lower-order modes, wave energy is nearly uniform radially due to their simplicity, with negligible geometric-operator coupling. As the mode order increases, the Legendre component of the eigenfunction exhibits higher radial oscillation frequencies. Combined with hyperbolic geometry, this effect progressively concentrates wave energy toward the boundaries.

The introduction of hyperbolic metrics reshapes the form of the Laplacian operator. In the conventional Euclidean space, the Laplacian operator Δ_E characterizes the diffusion behavior and wave attenuation process within a homogeneous medium. However, under the hyperbolic metric Δ_R, owing to alterations in geometric coefficients, the operator exhibits an “attraction” effect on boundaries: as $\rho \to 1$ or r_{in}, the value of the modified Laplacian operator converges to zero, thereby effectively constructing a potential well at the boundary. Consequently, the wave energy is compelled to remain confined within the boundary domain, thus realizing wave boundary localization.

4. Construction of the 3D model and spectral analysis

With the aforementioned theoretical predictions, we now construct an out-of-plane model based on the lattice points (240 points) of the type-II lattice after projection, as shown in Fig. 3(a), with $r_0 = 81.2$ mm, $R_0 = 174.9$ mm, $\theta = \pi/4$. As depicted in Fig. 3(b), the unit cell of the lattice is defined by the dimensions $t = 4$ mm and $d = 2$ mm. The material is 316L stainless steel with density $\rho_s = 8000\ \mathrm{kg/m^3}$, Young's modulus $E_s = 190$ GPa, and Poisson’s ratio $\mu_s = 0.26$. Using COMSOL Multiphysics software, we obtain the eigenspectra of the structure’s out-of-plane modes. The spectrum of the first 1000 eigenvalues is presented in Fig. 3(c), and the vibrational modes of the structure are categorized into four types. Mode 1 is bulk mode, while Modes 2 to 4 are boundary modes (Fig. 3(d)), which are concentrated in the frequency range from 56.67 kHz to 71.96 kHz. Notably, further calculations of high-frequency modes reveal a phenomenon of boundary aggregation, exemplified by the analysis of the first 1000 modes. These boundary modes are significantly more abundant than the type-I lattices, which only have a single type of boundary mode.

It is worth noting that the generation mechanism of these kind of boundary states are different from that of the topological boundary states generated by breaking time-reversal symmetry (Nieves et al., 2020). The boundary states in hyperbolic lattices stem from the non-Euclidean geometric properties. As the lattice order increases, the number of boundary sites becomes comparable to the total number of lattice sites. (Moran, 1997). It is this unique macroscopic geometric property that naturally enriches the energy spectrum with a large number of boundary states. Moreover, these boundary states are vulnerable to backscattering when they encounter defects.

To quantify the localization effect of these boundary states, we first divide the structure into three parts (Fig. 4(a)): the outer area ($0.85r_0 \le r \le r_0$), the bulk area ($0.55r_0 < r < 0.85r_0$), and the inner area $0.47r_0 \le r \le 0.55r_0$, and define the polarization index of boundary energy (*PE*) as

The subscripts ‘*inner*’ and ‘*outer*’ refer to the inner and outer regions of the structure respectively. The structure contains a total of 1928 discrete points, derived from an initial set of 240 lattice points. The parameter *PE* is used to quantify the imbalance between the vibrational energies of the inner and outer regions. When $PE \to -1$, the vibration mode is dominated by the inner region; conversely, when $PE \to 1$, the outer region dominates the mode (as shown in Fig. 4(c) and (e)). However, for $PE \to 0$, the vibrational energies of both

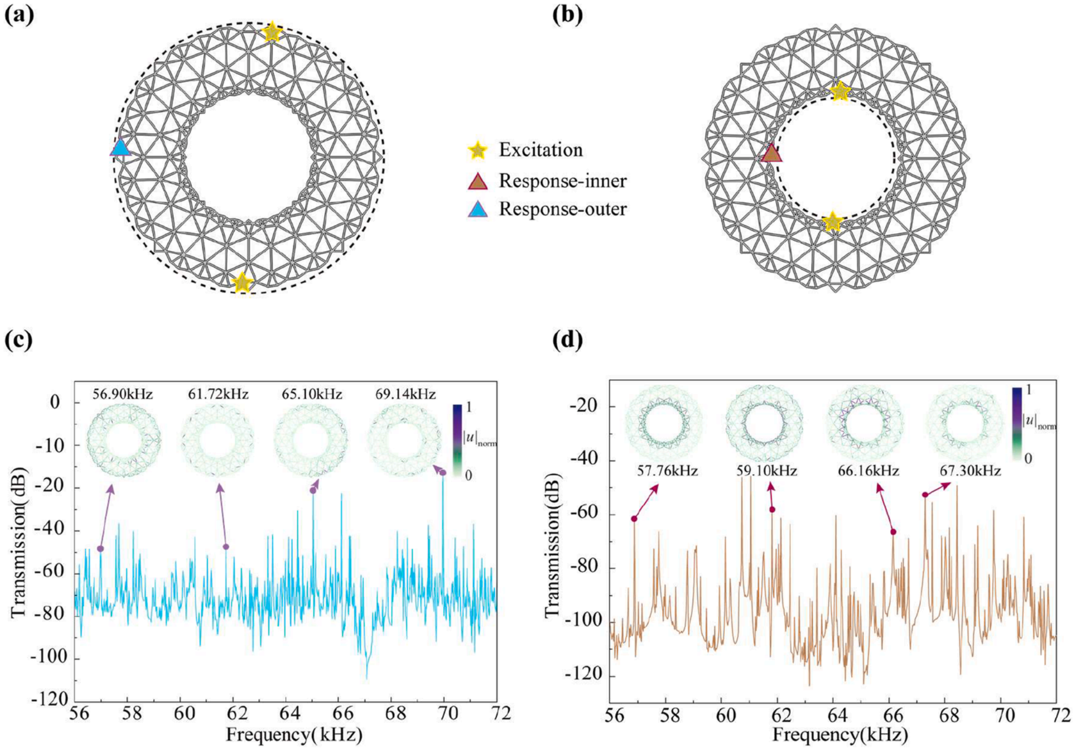

Fig. 5. Inner and outer ring transmission behavior. (a) and (b) represent diagonal excitations for the outer-ring mode and inner-ring mode. (c) and (d) present the transmission of response points under the excitations corresponding to the inner-ring and outer-ring modes. $|u|_{\mathrm{norm}}$ is the normalized displacement field.

regions are relatively balanced, making it challenging to distinguish between bulk modes and mixed boundary modes. To address this, we introduce the bulk energy ratio parameter (*BE*) to provide a further distinction,

$$BE = \frac{\sum_{i\in bulk} u_{bulk}^2(i)}{\sum_{i\in total} u_{total}^2(i)} \tag{13}$$

where the subscript '*bulk*' refers to the bulk region, and '*total*' refers to all regions. When *PE* is near zero, a smaller *BE* indicates a lower proportion of energy in the bulk region, suggesting that the structure exhibits a mixed state of inner and outer boundary modes (Fig. 3 (b) and (d)).

Next, we analyze the transport behavior of the structure using two-point excitation: inner-ring excitation (Fig. 5(a)) and outer-ring excitation (Fig. 5(b)). When each excitation is applied separately, Fig. 5(c) and (d) show that within the $56 - 72$ kHz range, the dominant peak in the response spectrum corresponds to the structural boundary mode. Notably, the distribution of these high-response boundary modes coincides with the aggregation of boundary states observed within the same frequency range in the eigenspectrum shown in Fig. 2(c). Furthermore, when examining the in-plane modes of the structure, a similar concentration of boundary states is observed, confirming the consistency of this behavior across different modes. Detailed results are provided in Appendix B.

5. Simulations of transient propagation of boundary states

The inner and outer boundary modes inherent to type-II hyperbolic rings provide a new approach for designing structural boundary protection against impact loading. Therefore, we conducted transient pulse simulations. The excitation function is defined as follows.

$$u(t) = \sin(2\pi f)e^{s_1(t-t_0)^2} \tag{14}$$

where $f = 64000$ Hz, $s_1 = -3\times10^{-8}$, $t_0 = 100$ μs. The Gaussian-modulated pulse function exhibits continuous and gradual temporal variations in its signal, characterized by a controllable frequency range and a concentrated energy distribution. It effectively mitigates spurious high-frequency interference induced by abrupt signal changes, thereby facilitating the investigation of structural pulse responses within specific frequency bands.

The pulse excitation has a step size of 1 μs and a duration of 1200 μs (Fig. 6(a)). Its frequency bandwidth ranges from 56 to 72 kHz, corresponding to the frequencies of the boundary modes (Fig. 6(b)). Under external pulse excitation (marked by a star in Fig. 6(c)), the boundary states of the structure are excited and evolve along the outer boundary path over time. At $t = 665$ μs, the edge modes

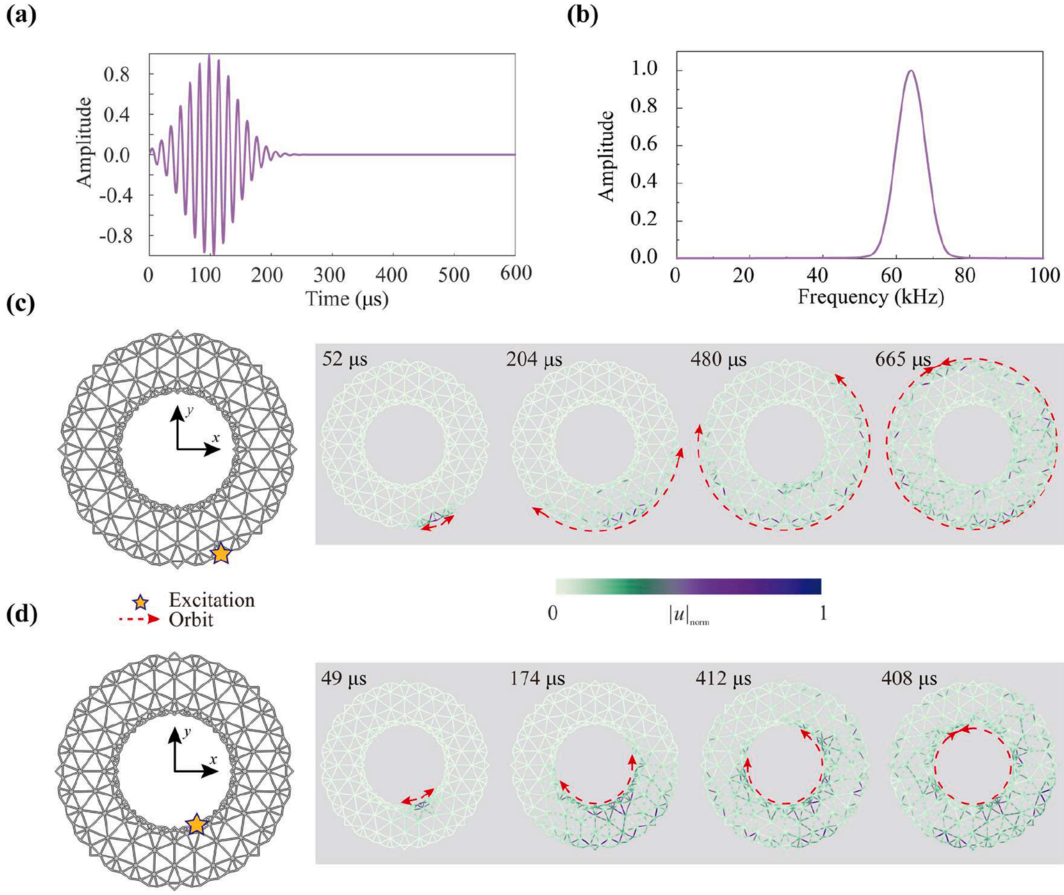

Fig. 6. Simulation of structural transient responses. (a) Time-domain signal of impulse excitation. (b) Frequency-domain signal of impulse excitation. (c) and (d) respectively depict the transient responses of the structure under external and internal excitations, with the red dashed line denoting the evolutionary trajectory of the boundary state as a function of time.

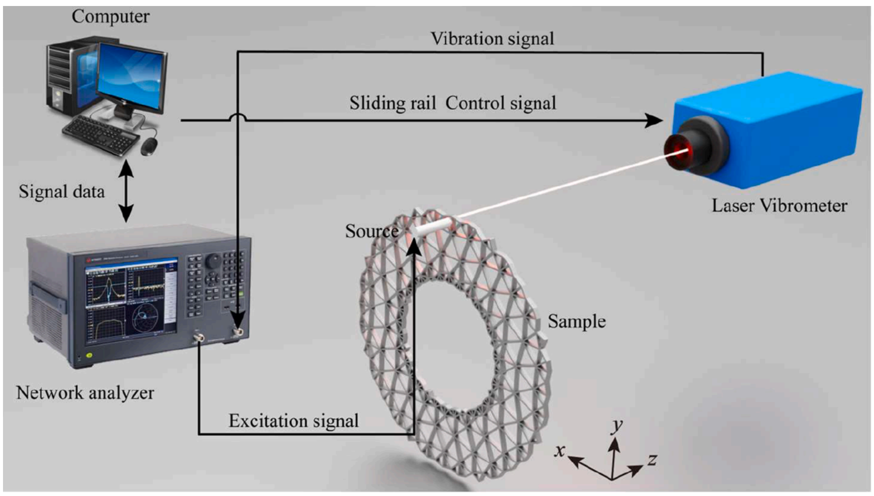

Fig. 7. Flowchart of frequency domain signal experiment.

propagate to the entire outer boundary of the structure. The red arrows explicitly denote the evolution process of boundary states in Fig. 6(c), highlighting the distinct instantaneous impulse responses of outer boundaries. Similarly, we apply the same excitation to the inner boundary, as shown in Fig. 6(d), and the edge modes propagate to the entire inner boundary at t = 408 μs. The transient

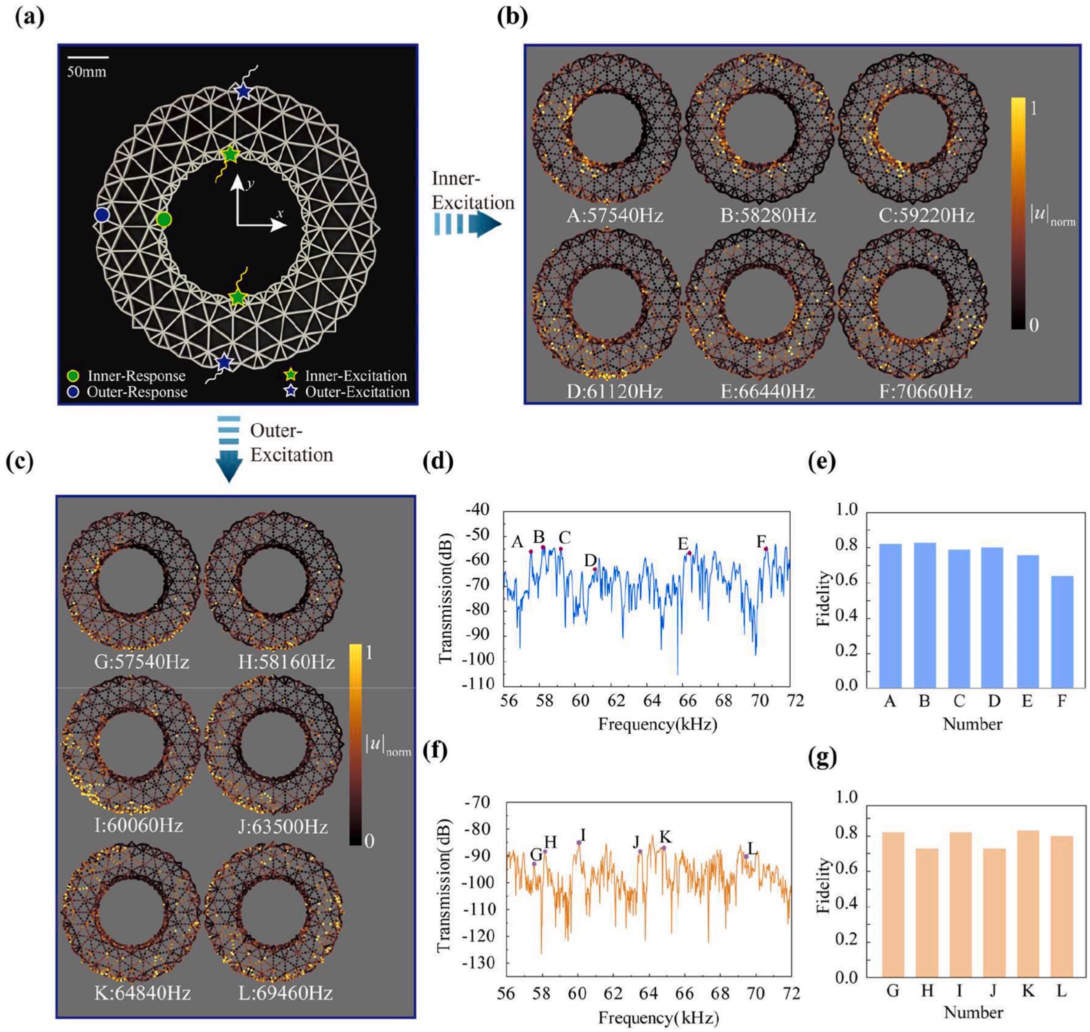

Fig. 8. Frequency response experiments on inner and outer boundary modes of type-II hyperbolic rings. (a) The 3D-printed sample. We designed two different diagonal excitation methods Inner-Excitation and Outer-Excitation and measured the response at the middle section of the structure. (b) and (c) depict the boundary displacement field distributions under distinct modal excitations. (d) Transmission of the structure under inner-boundary excitation, where A-F correspond to the experimental resonance peak frequencies. (e) Fidelity between experimental and simulated results of the inner boundary mode. (f) Transmission of the structure under Outer-Excitation, where G-L correspond to the experimental resonance peak frequencies. (g) Fidelity between experimental and simulated results of the Outer boundary mode.

responses of the two boundary modes demonstrate the potential advantages of type-II hyperbolic rings in impact protection. Under external disturbances, the inner and outer boundaries, guided by the hyperbolic metric, promote energy localization at the boundaries. This enables disturbances to dissipate along the boundaries, thereby protecting the structure's bulk region.

6. Experiment results

Based on previous theoretical and simulation results, we fabricated a real sample using 3D metal printing with 316L stainless steel. Piezoelectric ceramics served as point-like excitation sources, and response signals were measured using a laser interferometer. The frequency- and transient responses are presented in Section 6.1 and Section 6.2, respectively.

6.1. Frequency response experiments of type-II hyperbolic ring

The experiment setup and measurement are shown in Fig. 7. The sample was vertically placed. We used a vibration excitation source (P-845.6 preloaded piezoelectric ceramic actuator from PI company) to vertically excite the sample, aiming to excite the out-of-plane mode. The excitation signal of the excitation source was generated by a network analyzer (Keysight E5061B, output resistance 30 Ω), with a frequency range from 56 to 72 kHz, covering the entire frequency range of the boundary modes. The displacement field of

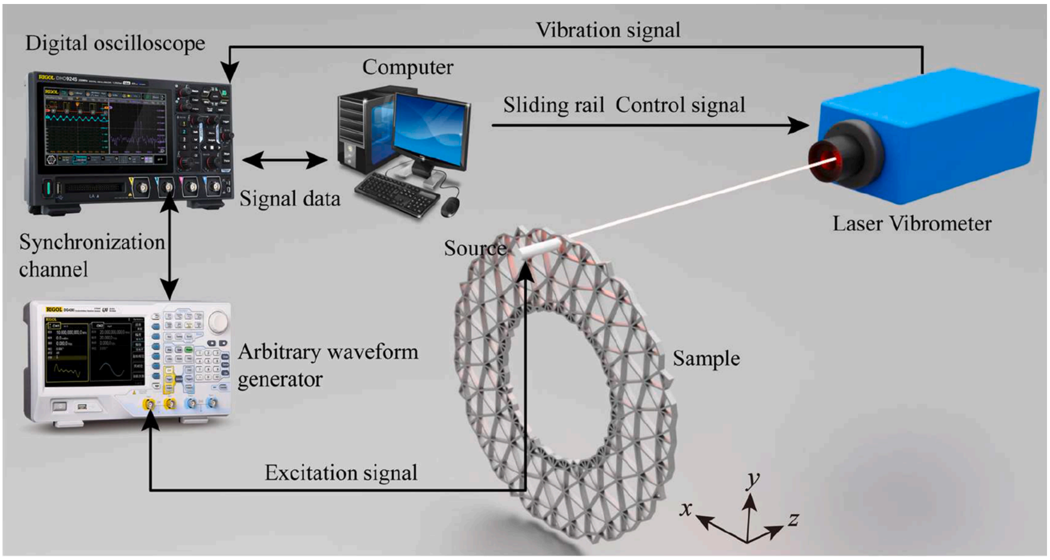

Fig. 9. Flowchart of time domain signal experiment.

the sample was measured with high accuracy using a laser vibrometer (Polytec OFV-5000) installed on a 2D automatic translation stage. The laser beam of the laser vibrometer was perpendicular to the sample, capturing only the vertical (z-axis) displacement component. During the scanning process, the computergenerated sliding rail signals to control the movement of the two-dimensional automatic translation stage, which drives the laser vibrometer to scan the surface of the sample according to the programmed movement route. The displacement signal recorded by the laser vibrometer was transmitted to the network analyzer and subsequently processed. All instruments were connected to a computer for real-time monitoring and data analysis.

Through the selection of distinct boundary excitation points (Fig. 8(a)), the corresponding structural vibration responses were measured. From the transmission spectrua (Fig. 8(d) and (f)), it can be observed that the structural vibration modes corresponding to the high peaks are in good agreement with the simulation results. The mode displacement field distributions corresponding to A-F and G-L are shown in Fig. 8(b) and Fig. 8(c), respectively. It is evident that distinct modal excitations have successfully stimulated the characteristic modes within the eigenspectrum, thereby demonstrating that the type-II hyperbolic ring possesses two kinds of boundary modes. In addition, to quantify the level of agreement between the experiment and simulation, the fidelity $F(f)$ is defined as (Lin et al., 2022).

$$F(f) = \frac{\left|\sum_{i=1}^{Num} \mathbf{u}_{\text{exp}}(i,f)\mathbf{u}^{*}_{\text{sim}}(i,f)\right|}{\sqrt{\left|\sum_{i=1}^{Num} \mathbf{u}_{\text{exp}}(i,f)\mathbf{u}^{*}_{\text{exp}}(i,f)\right|}\sqrt{\left|\sum_{i=1}^{Num} \mathbf{u}_{\text{sim}}(i,f)\mathbf{u}^{*}_{\text{sim}}(i,f)\right|}} \tag{15}$$

where $\mathbf{u}_{\text{exp}}$ and $\mathbf{u}_{\text{sim}}$ denote respectively the displacement fields in the experiment and simulation at frequency f, with $Num = 1928$. $F(f)$ is used to compare the degree of agreement between experiments and simulations. The value of F varies from 0 to 1. A higher F value indicates that the results of the experiment and the simulation are closer, reflecting the validity of the experiment. The calculated fidelities in our works are shown in Fig. 8(e) and (g). Most of these values are around 0.8. Experimental observations are in good agreement with simulations, apart from small deviations arising from fabrication inaccuracies. In addition, material damping leads to pronounced attenuation of elastic waves, further influencing the experimental results.

6.2. *Transient response experiments in type-II hyperbolic rings*

The experimental setup and measurements for the transient response experiments are shown in Fig. 9. We utilized an arbitrary waveform generator to generate the time-domain signal, as described in Eq. (14). The time interval was set as 0.8 μs, which enhances the measurement resolution. We also used a PI piezoelectric actuator as a point-like excitation source. The out-of-plane vibrations of the sample were measured by a laser vibrometer and transmitted to an oscilloscope to obtain time-domain signals. Meanwhile, the generator and the oscilloscope were connected via a synchronization channel to align the initial signals, thereby obtaining complete transient response signals at the measurement position. Finally, the data were transmitted to a computer for analysis.

The measured the time-domain signals of structural vibration using different boundary modes excitations are shown in Fig. 10. In Fig. 10(a), the signal propagating along the type-II outer boundary over time and the bulk containing weak signals. To further illustrate

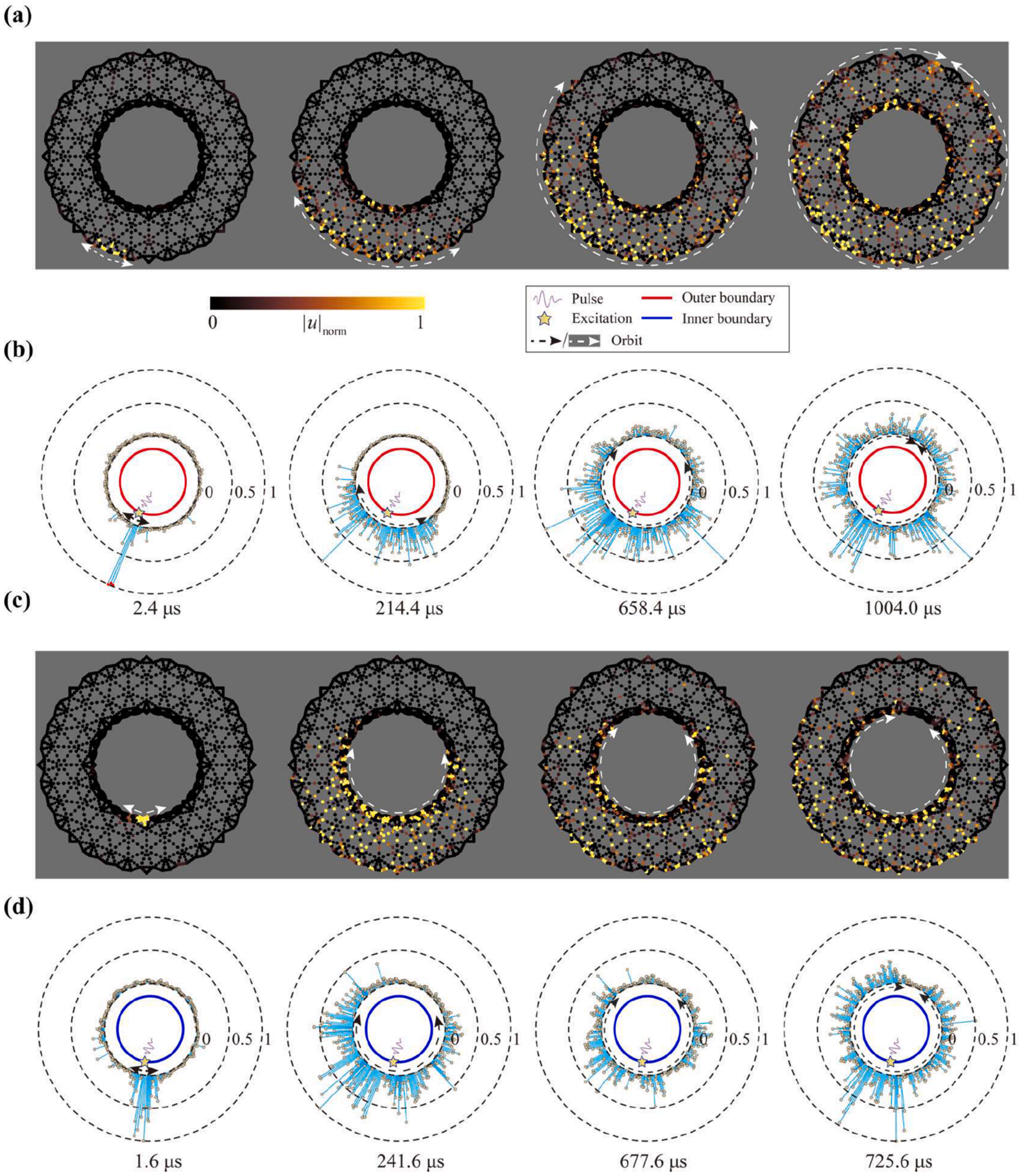

Fig. 10. Experiment on boundary transient time response. (a) The dynamic response of the structure under outer boundary excitation, with the white dashed lines representing the propagation trajectory of the boundary modes. (b) Normalized amplitude diagram of outer boundary points (320 points), where the pentagram indicates the outer boundary excitation with pulse. (c) The dynamic response of the structure under inner boundary excitation. (d) Normalized amplitude diagram of inner boundary points (320 points).

the boundary-localized response, we extracted 320 points from the outermost ring of the circular ring and plotted their normalized amplitudes in polar coordinates in Fig. 10(b). At 2.4 μs, the response of the structure is localized near the excitation point. At 1004 μs, the response had spread to the entire boundary, with its amplitude gradually decaying as the distance from the excitation source increases. In contrast, Fig. 10(c) presents the internal excitation, where the signal propagates along the inner boundary. The inner boundary mode arrives at the opposite side of the excitation source at 725.6 μs in Fig. 10(d). Transient excitations of the two modes trigger the evolution paths of the structure's internal and external boundary states, which are marked with black and white arrows in Fig. 10.

The evolution path of the external mode's boundary state exhibits a well-defined trajectory with distinct response characteristics, as explicitly indicated by the arrows. In contrast, the internal mode shows a weaker response and an indistinct propagation path. This behavior arises mainly from the lower proportion of inner boundary modes within the accessible frequency range, and the coupling between inner and outer modes in turn causes the stronger attenuation of elastic waves in the inner ring, both of which contribute to its reduced response. In addition, we also measured the transient response in the experiment on the in-plane modes of the structure in Appendix C. The results indicate that the in-plane vibration mode also exhibits a similar boundary transient response.

The dynamic inner and outer boundary responses in type-II hyperbolic rings evoke associations with impact protection designs based on structural boundary states. Leveraging this unique transmission phenomenon allows external disturbances to dissipate along the structural boundaries, thereby protecting the internal structure.

7. Conclusions

In this work, we have proposed a hyperbolic ring elastic metamaterial based on a type-II hyperbolic lattice, exploiting the fundamental features of hyperbolic geometry with constant negative curvature. Through interconnected lattice units, the structure redistributes elastic energy and localizes waves along diverging boundaries, thereby enabling distinctive wave manipulation capabilities. Its eigenmode distribution, frequency response, and transient transmission characteristics are systematically investigated through experiments and simulations. Governed by the hyperbolic metric, the structure naturally exhibits two kinds of boundaries with boundary states aggregated within specific frequency range (from 56 to 72 kHz). More importantly, transient response simulations and experiments consistently demonstrate that these states can propagate along either the inner or outer boundary, confining energy to the edges and protecting the interior region. This work expands elastic metamaterial design into hyperbolic space, introducing a non-Euclidean geometric approach for developing vibration-damping and impact-resistant materials.

In practical engineering, the proposed structure leverages its boundary state focusing effect to achieve excellent impact resistance and bidirectional protection in specific frequency bands, with broad application prospects. This hyperbolic lattice can be integrated into non-pneumatic tires to resist external disturbances; its inner-edge energy localization enables it to serve as a protective device for aero-engine casings and battery packs, circumferentially confining and dissipating internal impacts to block outward damage propagation. Furthermore, high-efficiency boundary vibration damping can be realized by deploying damping materials at energy-concentrated boundaries.

CRediT authorship contribution statement

Kailun Wang: Writing – original draft, Methodology, Investigation, Formal analysis. **Jingming Chen:** Investigation. **Yue Shen:** Investigation. **Xiang Li:** Writing – review & editing, Supervision, Funding acquisition, Formal analysis. **Zhen Gao:** Writing – review & editing, Supervision, Funding acquisition. **Ying Wu:** Writing – review & editing, Validation, Supervision, Investigation, Funding acquisition, Conceptualization.

Declaration of competing interest

The authors declare that they have no known competing financial interests or personal relationships that could have appeared to influence the work reported in this paper.

Acknowledgment

The authors wish to acknowledge the support from the National Natural Science Foundation of China (Grant Nos. 12302112, 12102193, 62375118, and 62361166627), the Fundamental Research Funds for the Central Universities (Grant No. 30923010207), Guangdong Basic and Applied Basic Research Foundation (Grant No.2024A1515012770), Shenzhen Science and Technology Innovation Commission (Grant Nos. 20220815111105001, and 202308073000209), High-level Special Funds (Grant No. G03034K004), and Postgraduate Research & Practice Innovation Program of Jiangsu Province (Grant No. KYCX25_0686).

Appendix A: Construction of type-II hyperbolic rings via conformal transformations

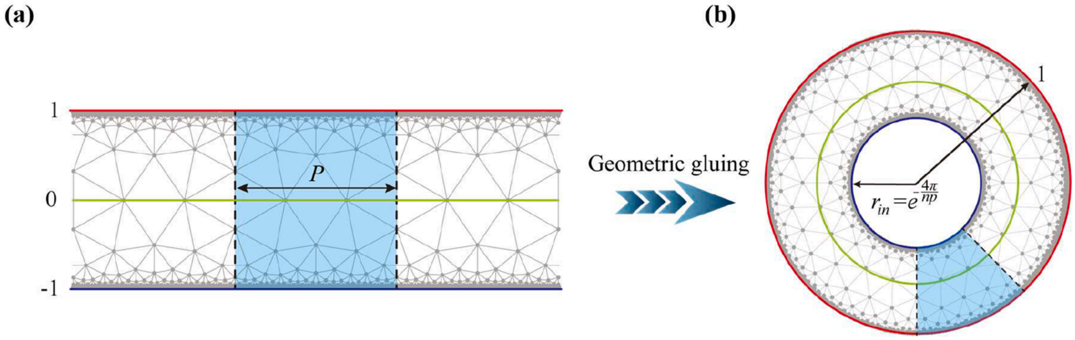

Fig. 11. The operational procedure of geometric gluing. (a) A hyperbolic band with discrete translational symmetry, from which the smallest repeating period $P = 1.845$ is intercepted. (b) Type-II hyperbolic ring, with $n = 8$.

We first consider the point z on the Poincaré disk ($\mathscr{D} = \{z = re^{I\theta},\ r < 1\}$) and perform the following transformation to map the disk into a hyperbolic band $\mathscr{B} = \{\zeta = r_b e^{I\theta_b},\ r_b < 1\}$.

$$z \mapsto \zeta(z) = \frac{2}{\pi}\ln\left(\frac{1+z}{1-z}\right) \tag{A1}$$

Subsequently, we extract the smallest repeating period ($P = 1.845$) from the hyperbolic band in Fig. 11(a) for transformation and perform geometric gluing to wrap it into a ring $\mathscr{R} = \{w = r_R e^{I\theta_R},\ r_{in} = e^{-\pi/r_h} < r_R < 1\}$ in Fig. 11(b), where $r_h = nP/4$.

$$\zeta \mapsto w(\zeta) = e^{I\frac{\pi}{2r_h}(\zeta+I)} \tag{A2}$$

Appendix B: Eigenspectrum and frequency-domain analysis of in-plane modes of the type-II hyperbolic lattice

To construct the in-plane model, the structural thickness along the z-direction (denoted as t) was increased as shown in Fig. 12(a), with the material remaining 316L stainless steel. The eigenspectrum of the first 1000 modes was calculated, revealing distinct boundary states within the frequency range of $60 - 100$ kHz (Fig. 12(b)). These boundary states include inner boundary modes, outer boundary modes, and mixed inner and outer boundary modes (Fig. 12(c)). Combined with the out-of-plane modes analyzed in Section 4, these results confirm that the hyperbolic space-projected geometric design inherently generates multi-boundary states, regardless of modal orientation. Notably, the in-plane mode configuration of the type-II hyperbolic ring exhibits conceptual parallels to cylindrical protective structures and non-pneumatic tires, thereby offering novel design principles for such engineering systems.

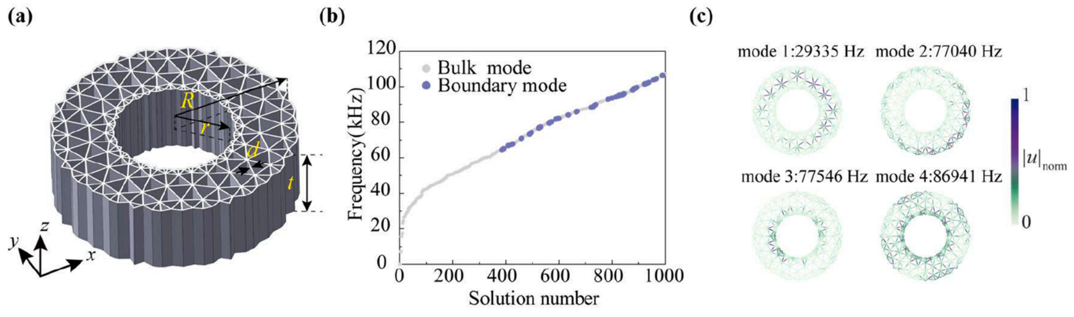

Fig. 12. 3D model and its eigenspectrum. (a) $\{3, 7, C_8\}$ type-II hyperbolic ring with $R = 50.4$ mm, $r = 23.5$ mm, $d = 0.7$ mm, and $t = 30$ mm. (b) The first 1000 orders of the eigenspectrum of the mode. (c) The two distinct boundary states in the eigenspectrum. Mode 1 is the bulk mode, mode 2 and mode 3 are the outer boundary mode and inner boundary mode respectively, and mode 4 is the mixed inner and outer boundary mode.

Frequency-domain analysis of in-plane modes was performed via linear excitation (yellow pentagrams in Fig. 13(a)), with excitation points applied along the z-direction to isolate in-plane vibrational behavior. The response spectrum (Fig. 13(b)) shows prominent peaks (A–D) corresponding to distinct boundary states, whose displacement fields are visualized in Fig. 13(c). However, compared to out-of-plane modes, in-plane modes exhibit more complex modal coupling, rendering their boundary states less readily excitable.

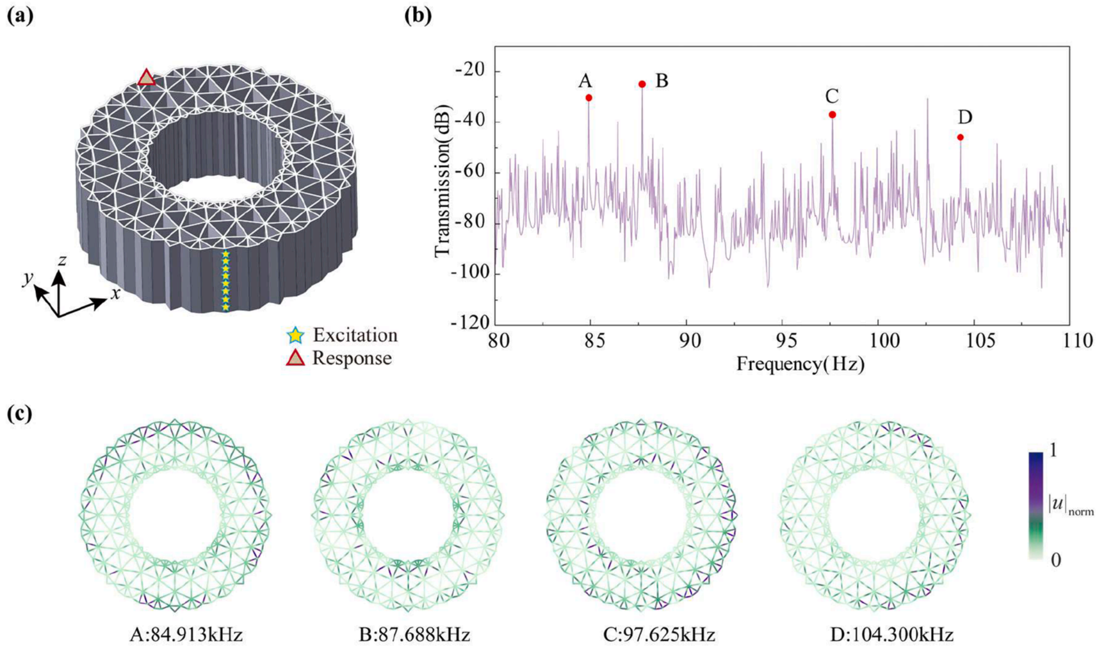

Fig. 13. Frequency domain analysis of the in-plane structure. (a) Excitation of the in-plane mode. To obtain the in-plane vibration modes of the structure, we employed a linear excitation in the simulation, distributed along the structural z-direction. (b) Transmission behavior at the response point, where Points A-D mark the peaks in the response spectrum. (c) Normalized displacement fields diagrams corresponding to these peak points.

Appendix C: Time-domain response of in-plane modes of the type-II hyperbolic lattice

We applied a pulse excitation to the side of the structure $u(t) = \sin(2\pi ft)e^{-8\times10^8\times(t-2\times10^{-5})}$, where $f = 62000$ Hz in Fig. 14. The simulated time-domain response (Fig. 14(b)) reveals boundary state propagation analogous to the out-of-plane mode in Section 5, where vibrational energy migrates along boundary paths from the excitation source to the opposite one. This confirms that in-plane modes also possess boundary-confined transmission capabilities, reinforcing the structure's potential for impact protection. Furthermore, we fabricated the sample shown in Fig. 14(c) using 3D printing. Three piezoelectric ceramics were used to simultaneously excite the sample on the side of the structure, aiming to stimulate the in-plane mode of the structure. The response diagram is shown in Fig. 14(d). At 4.8 μs, most of the vibrational energy remains localized at the excitation position. At 292.8 μs, the vibrational energy has gradually propagated along the outer boundary to the entire boundary of the structure. Measurement was limited to 240 points due to equipment precision constraints, with the structure's small thickness (only 0.7 mm) further impeding high-density sampling.

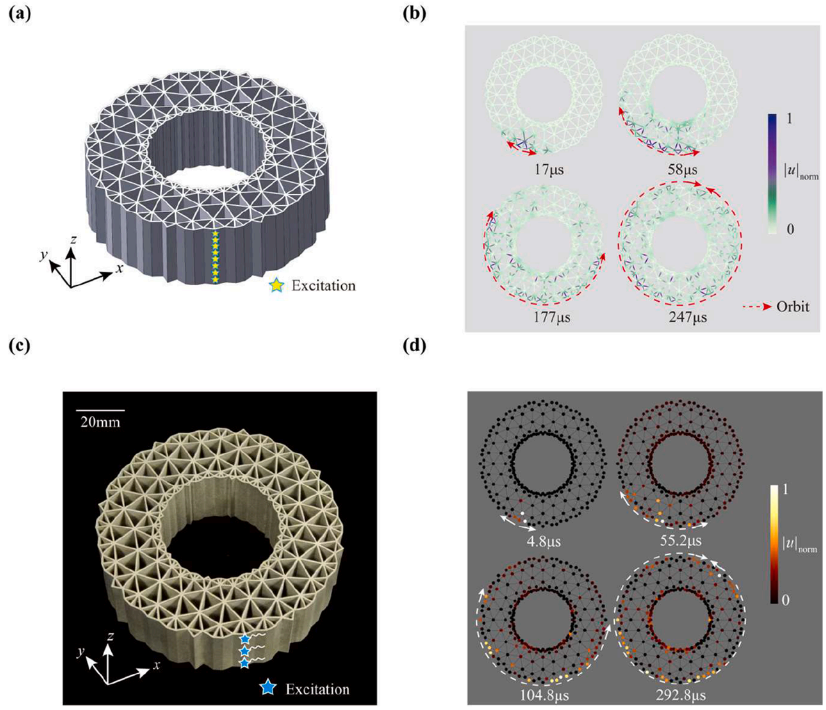

Fig. 14. Time-domain analysis of in-plane mode structures. (a) In the simulation analysis, line excitation is applied to the outer boundary of the structure. (b) The time-domain response of the structure in simulation. (c) 3D printed structural model. (d) The time-domain response of the structure in experiment.

Data availability

Data will be made available on request.

References

Anderson, J. W. (2005). *Hyperbolic geometry*. Springer-Verlag.
Bañados, M., Teitelboim, C., & Zanelli, J. (1992). Black hole in three-dimensional spacetime. *Physical Review Letters, 69*, 1849.
Berger, M. (2003). *A panoramic view of riemannian geometry*. Berlin, Heidelberg: Springer Berlin Heidelberg.
Bienias, P., Boettcher, I., Belyansky, R., Kollár, A. J., & Gorshkov, A. V. (2022). Circuit quantum electrodynamics in hyperbolic space: From photon bound states to frustrated spin models. *Physical Review Letters, 128*, Article 013601.
Boettcher, I., Bienias, P., Belyansky, R., Kollár, A. J., & Gorshkov, A. V. (2020). Quantum simulation of hyperbolic space with circuit quantum electrodynamics: From graphs to geometry. *Physical Review A, Atomic, Molecular, and Optical Physics, 102*, Article 032208.
Boettcher, I., Gorshkov, A. V., Kollár, A. J., Maciejko, J., Rayan, S., & Thomale, R. (2022). Crystallography of hyperbolic lattices. *Physical Review B, 105*, Article 125118.
Chen, Y., Yin, Y., Lin, Z. K., Zheng, Z. H., Liu, Y., Li, J., Jiang, J. H., & Chen, H. (2022). Observation of topological p -orbital disclination states in non-Euclidean acoustic metamaterials. *Physical Review Letters, 129*, Article 154301.
Chen, A., Brand, H., Helbig, T., Hofmann, T., Imhof, S., Fritzsche, A., Kießling, T., Stegmaier, A., Upreti, L. K., Neupert, T., Bzdušek, T., Greiter, M., Thomale, R., & Boettcher, I. (2023). Hyperbolic matter in electrical circuits with tunable complex phases. *Nature Communications, 14*, 622.

Chen J., Chen F., Yang L., Yang Y., Chen Z., Wu Y., Yan B., Xi X., Zhu Z., Cheng M., Liu G.G., Shum P.P., Chen H., Cai R.G., Yang R.Q., Yang Y., and Gao Z., AdS/CFT correspondence in hyperbolic lattices, ArXiv:2305.04862 (2023).
Chen, Q., Zhang, Z., Qin, H., Bossart, A., Yang, Y., Chen, H., & Fleury, R. (2024). Anomalous and Chern topological waves in hyperbolic networks. *Nature Communications, 15*, 2293.
Chen, J., Yang, L., & Gao, Z. (2025). Dynamic transfer of chiral edge states in topological type-II hyperbolic lattices. *Communications Physics, 8*, 97.
Cheng, N., Serafin, F., McInerney, J., Rocklin, Z., Sun, K., & Mao, X. (2022). Band theory and boundary modes of high-dimensional representations of infinite hyperbolic lattices. *Physical Review Letters, 129*, Article 088002.
Coxeter H.S.M., Regular and semi-regular polytopes. III, Math. Z. 200, 3 (1988).
Cui, Z., Wu, C., Wei, Q., Yan, M., & Chen, G. (2024). On-chip elastic wave manipulations based on synthetic dimension. *Physical Review Letters, 133*, Article 256602.
Dang, X., Feng, F., Duan, H., & Wang, J. (2022). Theorem on the compatibility of spherical kirigami tessellations. *Physical Review Letters, 128*, Article 035501.
Dey, S., Chen, A., Basteiro, P., Fritzsche, A., Greiter, M., Kaminski, M., Lenggenhager, P. M., Meyer, R., Sorbello, R., Stegmaier, A., Thomale, R., Erdmenger, J., & Boettcher, I. (2024). Simulating holographic conformal field theories on hyperbolic lattices. *Physical Review Letters, 133*, Article 061603.
Fang, X., Yu, D., Wen, J., Dai, Y., Begley, M. R., Gao, H., & Gumbsch, P. (2025). Large recoverable elastic energy in chiral metamaterials via twist buckling. *Nature, 639*, 639–645.
Harvey, M. (2016). *Geometry illuminated: An illustrated introduction to Euclidean and hyperbolic plane geometry, 53*. University of Virginia.
Hilbert, D. R. (1890). Ueber die theorie der algebraischen formen. *Mathematische Annalen, 36*, 473–534.
Hong, Y., Chi, Y., Wu, S., Li, Y., Zhu, Y., & Yin, J. (2022). Boundary curvature guided programmable shape-morphing kirigami sheets. *Nature Communications, 13*, 530.
Huang, L., He, L., Zhang, W., Zhang, H., Liu, D., Feng, X., Liu, F., Cui, K., Huang, Y., Zhang, W., & Zhang, X. (2024). Hyperbolic photonic topological insulators. *Nature Communications, 15*, 1647.
Huang, L., Zhang, W., Zong, Y., He, L., & Zhang, X. (2025). Hyperbolic topological frequency combs. *ACS Photonics, 12*, 219.
Kollár, A. J., Fitzpatrick, M., & Houck, A. A. (2019). Hyperbolic lattices in circuit quantum electrodynamics. *Nature, 571*, 45.
Kollár, A. J., Fitzpatrick, M., Sarnak, P., & Houck, A. A. (2020). Line-graph lattices: Euclidean and non-Euclidean flat bands, and implementations in circuit quantum electrodynamics. *Communications in Mathematical Physics, 376*, 1909.
Lei, Y., Wang, Y., Cui, R., Huang, X., Zhang, L., Jin, Y., Gao, J., & Deng, B. (2025). 3D hyperbolic kirigami metamaterials with tunable auxeticity and multistability. *Advancement of Science*, Article e06703.
Lenggenhager, P. M., Stegmaier, A., Upreti, L. K., Hofmann, T., Helbig, T., Vollhardt, A., Greiter, M., Lee, C. H., Imhof, S., Brand, H., Kießling, T., Boettcher, I., Neupert, T., Thomale, R., & Bzdušek, T. (2022). Simulating hyperbolic space on a circuit board. *Nature Communications, 13*, 4373.
Li, X., Chua, J. W., Yu, X., Li, Z., Zhao, M., Wang, Z., & Zhai, W. (2024). 3D-printed lattice structures for sound absorption: Current progress, mechanisms and models, structural-property relationships, and future outlook. *Advancement of Science, 11*, Article 2305232.
Lin, Z. K., Wu, Y., Jiang, B., Liu, Y., Wu, S. Q., Li, F., & Jiang, J. H. (2022). Topological Wannier cycles induced by sub-unit-cell artificial gauge flux in a sonic crystal. *Nature Materials, 21*, 430.
Ma, W. W. S., Yang, H., Zhao, Y., Li, X., Ding, J., Qu, S., Liu, Q., Hu, Z., Li, R., Tao, Q., Mo, H., Zhai, W., & Song, X. (2025). Multi-physical lattice metamaterials enabled by additive manufacturing: Design principles, interaction mechanisms, and multifunctional applications. *Advancement of Science, 12*, Article 2405835.
Maciejko, J., & Rayan, S. (2021). Hyperbolic band theory. *Science Advances, 7*, eabe9170.
Moran, J. F. (1997). The growth rate and balance of homogeneous tilings in the hyperbolic plane. *Discrete Mathematics, 173*, 151–186.
Nieves, M. J., Carta, G., Pagneux, V., & Brun, M. (2020). Directional Control of rayleigh wave propagation in an elastic lattice by gyroscopic effects. *Frontiers in Materials, 7*, Article 602960.
Patino, N. H., Rasmussen, C., & Ruzzene, M. (2024). Hyperbolic-space spectral characteristics for a network of mechanical linkages. *Physical Review Applied, 22*, Article 014048.
Patino, N. H., Lomazzi, L., De Beni, L., & Ruzzene, M. (2025). Elastic hyperbolic strip lattices. *Physical Review Applied, 24*, Article 014016.
Petermann, E., & Hinrichsen, H. (2024). Eigenmodes of the Laplacian on hyperbolic lattices. *Physical Review D, 109*, Article 106019.
Poincaré, H. (1882). Mémoire sur les courbes définies par une équation différentielle. *Journal de Mathématiques Pures et Appliquées, 8*, 251.
Qin, H., Zhang, W., & Zhang, X. (2024). Boundary-dominated photonic Chern insulators with hyperbolic lattice geometry. *Physical Review B, 110*, Article 155123.
Ren, X., Das, R., Tran, P., Ngo, T. D., & Xie, Y. M. (2018). Auxetic metamaterials and structures: A review. *Smart Materials and Structures, 27*, Article 023001.
Ruzzene, M., Prodan, E., & Prodan, C. (2021). Dynamics of elastic hyperbolic lattices. *Extreme Mechanics Letters, 49*, Article 101491.
Song, Z., Wu, K., Wang, Z., He, L., & Ni, Y. (2024). Fracture mechanics of bi-material lattice metamaterials. *Journal of the Mechanics and Physics of Solids, 192*, Article 105835.
Tung, M. M., & Weinmüller, E. B. (2019). Acoustic metamaterial models on the (2+1)D Schwarzschild plane. *Journal of Computational and Applied Mathematics, 346*, 162.
Tung, M. M. (2018). Modelling acoustics on the Poincaré half-plane. *Journal of Computational and Applied Mathematics, 337*, 366.
Waitukaitis, S., Dieleman, P., & Van Hecke, M. (2020). Non-Euclidean origami. *Physical Review E, 102*, Article 031001.
Wang, Y., & Ren, J. (2023). Holographic complexity of hyperbolic black holes. *Physical Review D, 108*, Article 046006.
Wang, H., Xiu, X., Wang, Y., Xue, Q., Ju, W., Che, W., Liao, S., Jiang, H., Tang, M., Long, J., & Hu, J. (2020). Paper-based composites as a dual-functional material for ultralight broadband radar absorbing honeycombs. *Composites Part B: Engineering, 202*, Article 108378.
Wu, Y., Lu, J., Huang, X., Yang, Y., Luo, L., Yang, L., Li, F., Deng, W., & Liu, Z. (2023). Topological materials for full-vector elastic waves. *National Science Review, 10*, nwac203.
Yang, L., Wu, Y., Yu, K., Zhao, R., Wang, W., Bonello, B., & Djafari-Rouhani, B. (2022). Robust Fano resonance between mechanical first- and second-order topological states. *International Journal of Mechanical Sciences, 236*, Article 107768.
Yuan, H., Zhang, W., Pei, Q., & Zhang, X. (2024). Hyperbolic topological flat bands. *Physical Review B, 109*, Article L041109.
Zhang, W., Yuan, H., Sun, N., Sun, H., & Zhang, X. (2022). Observation of novel topological states in hyperbolic lattices. *Nature Communications, 13*, 2937.
Zhang, W., Di, F., Zheng, X., Sun, H., & Zhang, X. (2023). Hyperbolic band topology with non-trivial second Chern numbers. *Nature Communications, 14*, 1083.
Zheng, Z., & Chen, Y. (2023). Defect-controlled topological edge states in the curved acoustic lattices. *Europhysics Letters, 141*, Article 55002.